The Transition Region and Coronal Explorer

B. N. HANDY, L. W. ACTON and C. C. KANKELBORG
Department of Physics, Montana State University—Bozeman, P.O. Box 173840, Bozeman, Montana 59717 USA

C. J. WOLFSON, D. J. AKIN, M. E. BRUNER, R. CARAVALHO, R. C. CATURA, R. CHEVALIER, D. W. DUNCAN, C. G. EDWARDS, C. N. FEINSTEIN, S. L. FREELAND, F. M. FRIEDLAENDER, C. H. HOFFMANN, N. E. HURLBURT, B. K. JURCEVICH, N. L. KATZ, G. A. KELLY, J. R. LEMEN, M. LEVAY, R. W. LINDGREN, D. P. MATHUR, S. B. MEYER, S. J. MORRISON, M. D. MORRISON, R. W. NIGHTINGALE, T. P. POPE, R. A. REHSE, C. J. SCHRIJVER, R. A. SHINE, L. SHING, K. T. STRONG, T. D. TARBELL, A. M. TITLE and D. D. TORGERSON
Lockheed Martin Palo Alto Advanced Technology Center, O/L9-41, B-252, 3251 Hanover Street, Palo Alto, California 94304 USA

L. GOLUB, J. A. BOOKBINDER, D. CALDWELL, P. N. CHEIMETS, W. N. DAVIS, E. E. DELUCA, R. A. MCMULLEN and H. P. WARREN
Smithsonian Astrophysical Observatory, 60 Garden Street, Cambridge, Massachusetts 02138 USA

D. AMATO, R. FISHER, H. MALDONADO and C. PARKINSON
NASA/Goddard Space Flight Center, Greenbelt, Maryland 20771 USA

Abstract. The *Transition Region and Coronal Explorer* (TRACE) satellite, launched 2 April 1998, is a NASA Small Explorer (SMEX) that images the solar photosphere, transition region and corona with unprecedented spatial resolution and temporal continuity. To provide continuous coverage of solar phenomena, TRACE is located in a sun-synchronous polar orbit. The $\sim$ 700 Mbytes of data which are collected daily are made available for unrestricted use within a few days of observation.

The instrument features a 30 cm Cassegrain telescope with a field of view of 8.5 × 8.5 arc minutes and a spatial resolution of 1 arc second (0.5 arc second pixels). TRACE contains multilayer optics and a lumogen-coated CCD detector to record three EUV wavelengths and several UV wavelengths. It observes plasmas at selected temperatures from 6 000 K to 10 MK with a typical temporal resolution of less than one minute.

© 1999 *Kluwer Academic Publishers. Printed in the Netherlands.*

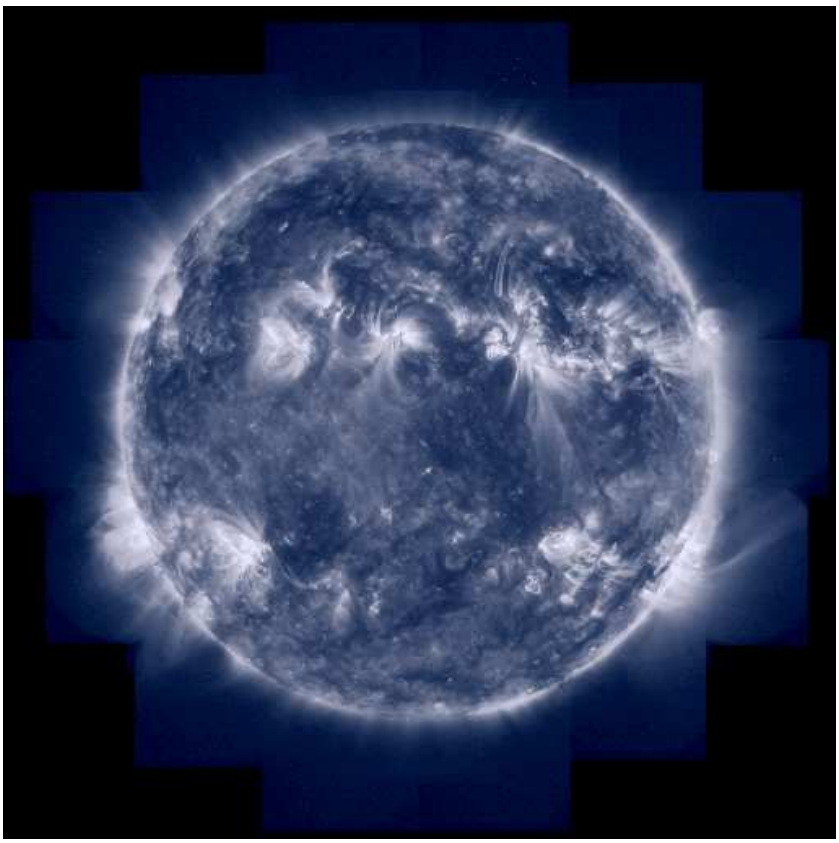

Figure 1. A TRACE full-disk mosaic of the Fe IX/X lines at 171 Å, taken 10-Oct-1998. The image is scaled to square root of intensity, and is composed of 42 individual repointings of the instrument.

1. Introduction

The *Transition Region and Coronal Explorer* (TRACE) investigation explores the dynamics and evolution of the solar atmosphere from the photosphere to the corona with high spatial and temporal resolution (Strong et al., 1994; Tarbell et al., 1994; Golub et al., 1999). Normal incidence multilayer optics capable of observing from the photosphere to the corona enable TRACE to follow the evolution and dynamics of the solar atmosphere at selected temperatures over the range 6 000K–10MK (table I; also figure 1).

The TRACE observatory is a single-instrument spacecraft in a polar orbit roughly following the day-night terminator. This allows

for continuous uninterrupted solar observing for approximately 9 months each year. For the remaining 3 month eclipse season, the view from part of the TRACE orbit is occulted by the earth. It was mated to a Small Explorer (SMEX) spacecraft and launched on 2 April 1998 from Vandenberg Air Force Base on a Pegasus XL launch vehicle (Orbital Sciences Corporation).

Table I. TRACE Temperature Response

Wavelength (Å)	Emission	Bandwidth (Å)	Temperature (K)
171	Fe IX/X	6.4	$1.6–2.0\times10^5$
195	Fe XII/XXIV	6.5	$5.0–20\times10^5$, $1.1–2.6\times10^7$
284	Fe XV	10.7	$1.25–4.0\times10^6$
1216	H I Ly α	84	$1.0–3.0\times10^4$
1550	C IV	30	$6.0–25\times10^4$
1600	UV Cont, C I, Fe II	275	$4.0–10\times10^3$
1700	Continuum	200	$4.0–10\times10^3$
5000	White Light	broad	$4.0–6.4\times10^3$

The TRACE instrument employs heritage from several previous satellite and sounding rocket programs. The *Normal Incidence X-ray Telescope* (NIXT, Golub et al., 1990) rocket payload had taken the highest resolution EUV coronal images prior to TRACE and the EUV optics in TRACE were provided by the NIXT team. Similar normal-incidence EUV multilayer coatings were successfully employed on the Stanford Multi-Spectral Solar Telescope (MSSTA, Walker et al., 1990; Barbee et al., 1991). The team that provided the Michelson Doppler Imager (MDI, Scherrer et al., 1995) for the *Solar & Heliospheric Observatory* (SOHO, Domingo et al., 1995) provided many of the designs for components used on TRACE, and some of the TRACE flight hardware items are MDI flight spares. The quadrant design of TRACE is much like that of the Extreme-ultraviolet Imaging Telescope (EIT, Delaboudinière et al., 1995). TRACE also uses EUV coatings similar to those on the EIT instrument. The UV optics and the C IV data reduction algorithms are based in part on experience from the *Solar Plasma Diagnostic Experiment* (SPDE, Damè et al., 1996).

2. The Instrument

The TRACE telescope is a Cassegrain design with a 30 cm aperture and a field of view of 8.5 × 8.5 arc minutes, equivalent to one-tenth of the solar disk (table II). The telescope is divided into four quadrants, each of which is defined for a specific wavelength band by segmented multilayer coatings on matching quadrants of the primary and secondary mirrors. The resolution of the instrument is Nyquist-limited by the CCD detector to 1 arc second (0.5 arc second pixels), and the focused image is recorded on a phosphor-coated CCD sensitive to ultraviolet (UV) and extreme ultraviolet (EUV) wavelengths.

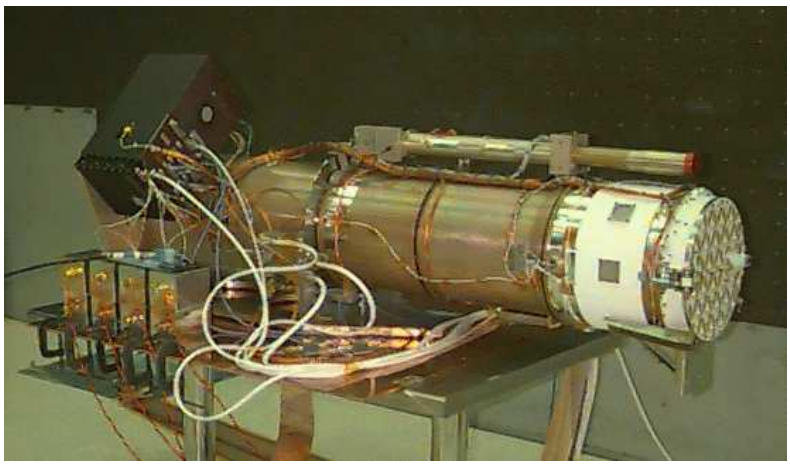

Figure 2. The TRACE instrument during testing. The entrance to the telescope is at the right of the picture. The guide telescope is visible at the top of the main telescope. The data processing unit (DPU) is temporarily mounted to the aft end of the instrument.

The telescope is pointed through the use of a guide telescope and limb sensor, visible on top of the main telescope in figure 2. Wavelength selection is determined by a quadrant selector located just behind the entrance filter chamber (see figure 3). The bandpass is defined by multilayer coatings on the primary and secondary mirrors (detailed in section 2.1). Filters are mounted at the entrance of the telescope to reduce visible and stray light inside the telescope, and a pair of filter wheels are mounted behind the primary mirror to further filter the beam and provide wavelength selection in the UV channel. The two filter wheel assemblies are flight spares from the MDI instrument. One position in each wheel

Table II. The TRACE instrument at a glance.

Mirrors	Multilayer-coated ULE
Primary diameter	30 cm
Effective focal length	8.66 m
Field of view	8.5×8.5 arc minutes
Resolution	1 arc second
CCD Detector	1024×1024, 3-phase, MPP, unthinned, partially inverted, front-illuminated
Phosphor Coating	lumogen
Pixel size	21 μm (0.50 arc seconds)
Full Well	450,000 electrons
Pointing Stability	0.1 arc second RMS
Payload Mass	36 kg
Payload Power	69 W
Scientific Telemetry	$\approx$ 700 Mbyte/day

is equipped with a thin-film Al filter to provide further stray light attenuation in the case of pinholes or some other form of failure in the entrance filters. Two locations in each filter wheel contain filters to select passbands in the UV wavelengths, and the remaining position in each wheel is open.

The exposure time is controlled via a shutter mechanism. The shutter blade has two openings, providing two ranges of exposure times: a small opening provides multiples of a 1.6 ms exposure time by making multiple passes across the CCD. Longer exposures are accomplished with a wide opening that exposes the entire CCD at once and is left open for the duration of the exposure from 20 ms to 260 s.

2.1. Optics

The TRACE optical path is composed of a set of entrance filters, a matched set of thin-film multilayer coatings on two normal-incidence mirrors, two filter wheels behind the primary mirror and a lumogen-coated CCD detector.

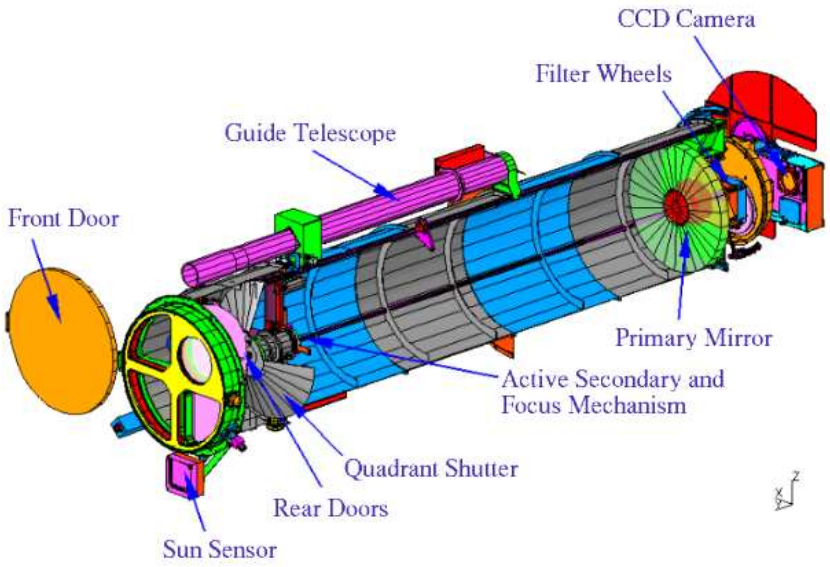

Figure 3. An isometric diagram of the TRACE telescope.

The instrument is divided into quadrants, with each quadrant carrying optics optimized for a specific wavelength: 171, 195, and 284 Å for the three EUV quadrants, and a range of 1200–7000 Å for the UV quadrant. A description of the various sections of the optical path follows.

2.1.1. *Entrance Filter Assembly*
Visible light is excluded from the telescope in the EUV quadrants by three thin-film Aluminum filters and in the UV quadrant by a broadband UV filter. These filters are mounted in the filter chamber assembly (FCA). The FCA, shown in figure 4, was evacuated to $\lesssim$ 10 torr prior to launch to protect the EUV filters from damage by acoustic vibration during launch. It is an aluminum structure with a single front door and a pair of rear clamshell doors. Wax actuators are used to release the doors which subsequently open via a spring-loaded mechanism (Cheimets et al., 1998b).

The thin-film Al filters in the TRACE instrument were manufactured by Luxel Corporation. The entrance filters are the largest ever flown in space. They are composed of $Al_2O_3/Al/Al_2O_3/C$ with approximate thicknesses of 40, 1500, 20, and 50 Å, respec-

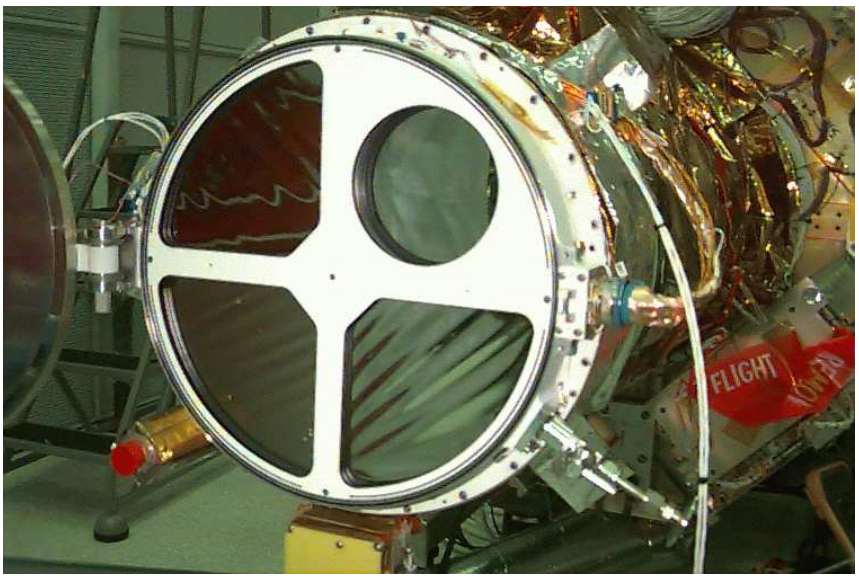

Figure 4. The Filter Chamber Assembly. The EUV filters are in the three triangular quadrants and the UV entrance filter is in the circular cutout. The front door is visible on the left.

tively. A pair of filters located in the focal plane are $Al_2O_3/Al/Al_2O_3$, with layers 40, 1500, and 40 Å thick. The thickness of the Al_2O_3 layer is approximate as it is the result of oxidation of the Aluminum film. The filters are supported on an opaque 70 line per inch Ni mesh, with has an intrinsic transmission of 82%. The transmissions of the Al filters are depicted in figure 5. The transmissions were modeled using IMD, a multilayer modeling library (Windt, 1998). The physical constants used in the model were derived from tables maintained by the Center of X-ray Optics at Lawrence Berkeley Laboratory and Lawrence Livermore National Laboratory (see appendix A).

The EUV filters were specified to provide visible light attenuation of 10^{-4} to satisfy heat and stray light requirements within the instrument. The filters were light-leak checked prior to integration with the instrument, and the measured transmission was found to be $< 8 \times 10^{-6}$ (Cheimets et al., 1998b). The front filters are periodically checked on-orbit for additional pinholes and stray light by measuring the light levels with the filter wheels in the open positions. After 8 months on orbit, including passage through

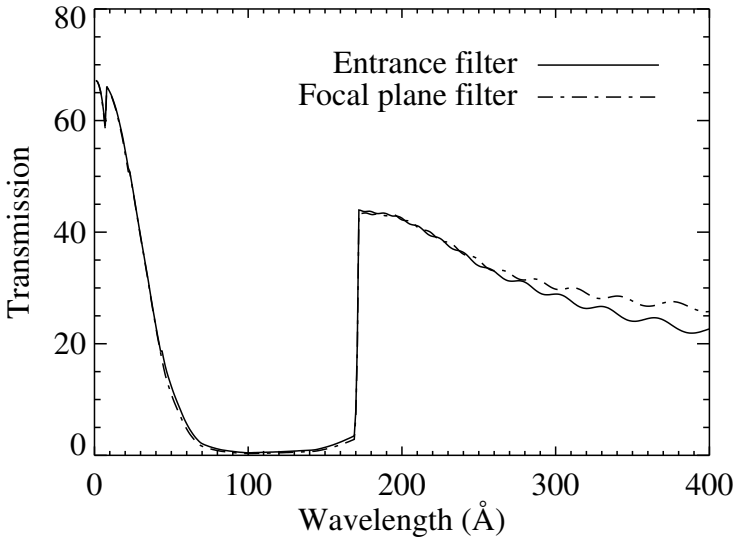

Figure 5. Modeled transmission of the EUV filters. The entrance filter is a thin film of $Al_2O_3/Al/Al_2O_3/C$ and the focal plane filters are $Al_2O_3/Al/Al_2O_3$. The transmission of the Nickel mesh (82%) is included in these curves. The entrance filter and one focal plane filter is used during a typical EUV exposure.

the Leonids Meteor Shower on 17 November 1998, the stray light transmission of the front filters is still $\lesssim 5 \times 10^{-6}$.

The UV entrance filter is a large 10 mm thick × 11.8 cm diameter substrate of MgF_2, coated with a broadband UV multilayer (see figure 6). This filter was coated by Acton Research Corporation (ARC). The purpose of this coating was to transmit as highly as possible at 1216 Å and 1550 Å while simultaneously rejecting UV continuum $\gtrsim$ 1600 Å and suppressing long-wavelength contamination. The response is shown in figure 6.

2.1.2. *Mirrors*

The primary and secondary mirrors have matched coatings in each of the four quadrants. Three of these quadrants are coated for wavelengths in the EUV and the fourth is coated for observations in the UV.

The TRACE mirrors substrates are Ultra-Low Expansion glass (ULE, Corning Glass Co.). They were ground and figured by Wilc Instruments to $\lambda/80$ at 6300 Å. The mirrors were then superpol-

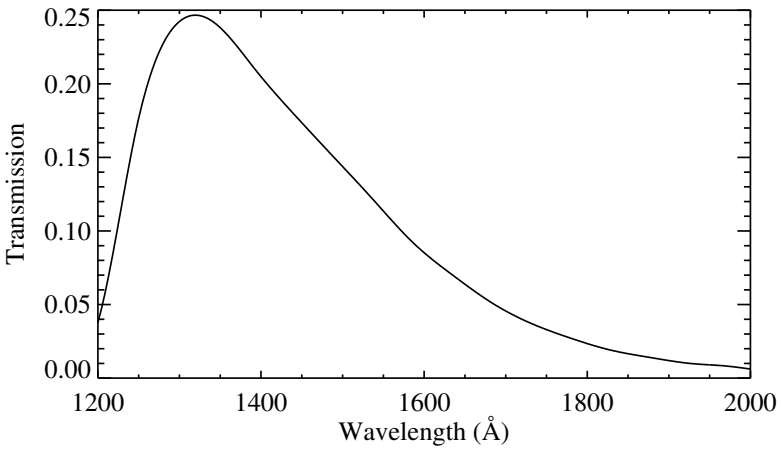

Figure 6. The transmission of the UV entrance filter. The filter is a multilayer dielectric coating on a MgF_2 substrate, optimized to transmit the resonance lines at λ 1216 Å and 1550 Å. The filter blocks long-wavelength ($\gtrsim$ 2000 Å) continuum but sufficient light leaks through to generate a useful "white light" image.

ished by Hughes Danbury Corp. to a roughness of approximately 7 Å RMS. The surface roughness was measured with an Atomic Force Microscope (AFM) at Digital Instruments, Inc. This surface smoothness was required for satisfactory reflectivity of the EUV coatings. The optics were then cleaned by General Optics, Inc. prior to coating. The coatings for the three EUV quadrants on each mirror were applied at Lawrence Livermore National Laboratory (LLNL). The mirrors were then shipped to ARC who subsequently coated the UV quadrant. The mirrors were integrated into the instrument at the Lockheed Martin Solar & Astrophysics Laboratory (Cheimets et al., 1998a).

The combined EUV response of the primary and secondary mirrors is shown in figure 7. The Mo_2C/Si multilayer coatings produced at LLNL for this telescope have the highest reflectivities ever flown at these wavelengths with such a narrow bandpass (table I). The primary and secondary mirror EUV reflectivities were measured at Lucent Technologies and NIST, respectively.

The UV quadrant mirrors use a combination of two different types of coatings (see figure 8). The primary mirror is coated with an all-dielectric multilayer, selected to favor the λ 1550 Å C IV

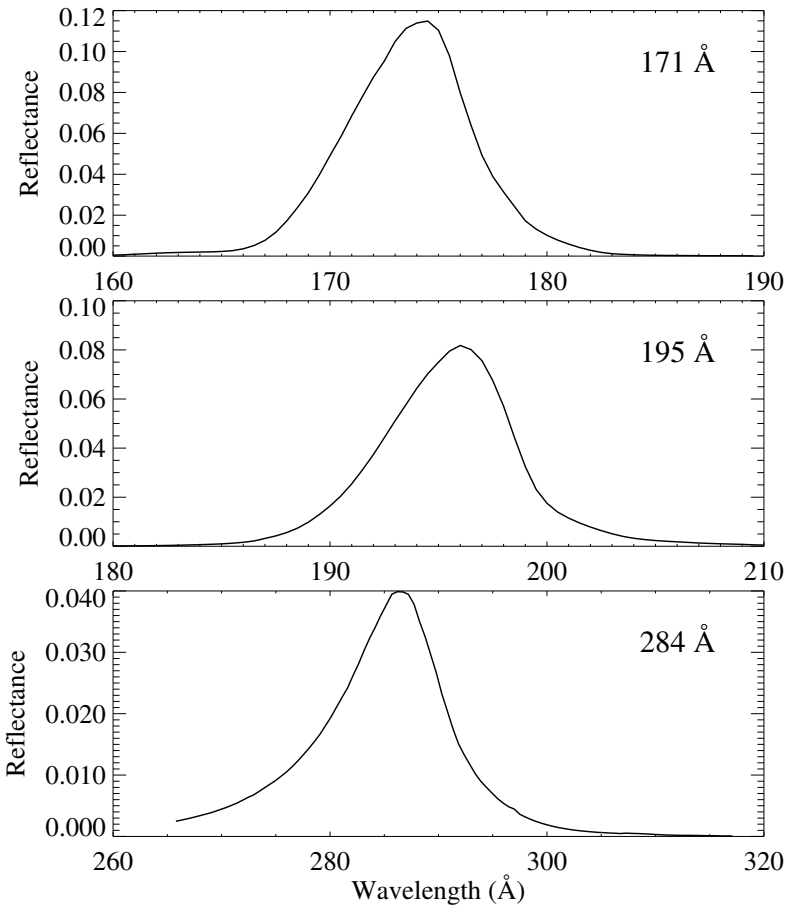

Figure 7. Combined EUV reflectivities for the primary and secondary mirrors.

emission lines and reduce light levels and thermal load on the secondary mirror. The secondary mirror is coated with Al and MgF_2. This combination enables observation of both the 1216 Å and 1550 Å emission lines. The coatings were developed by ARC.

2.1.3. *Focal plane filters*

A pair of filter wheels in front of the focal plane fulfill different roles for the EUV and UV channels. In the EUV, thin film Al filters are used to prevent stray visible light (due to pinholes in the entrance filter) from reaching the CCD detector. Two filters are provided for this purpose, one in each filter wheel. Typically

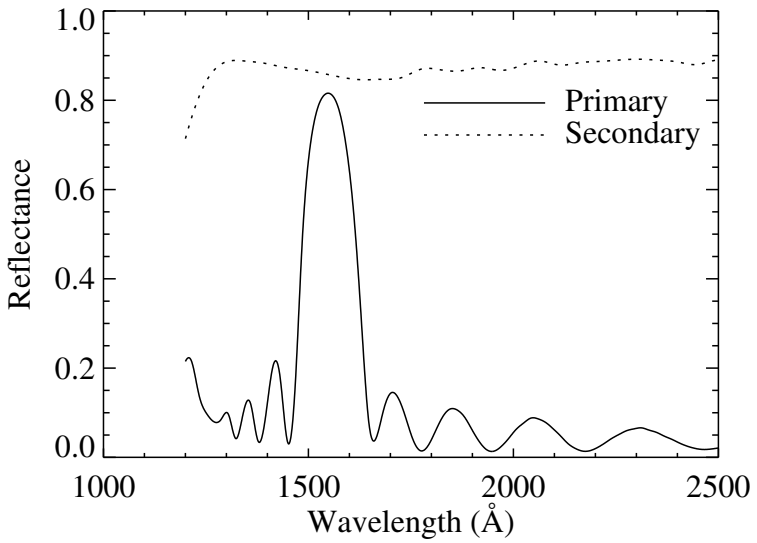

Figure 8. Primary and secondary mirror response curves for the UV quadrant. The primary mirror is coated with an all-dielectric multilayer coating optimized for the 1550 Å resonance lines. The secondary mirror is coated with Aluminum and MgF_2.

one filter is used in tandem with the entrance filter to reject stray light.

Both filters are mounted with their mesh at 45 degrees to the axes of the CCD detector, because simulations have shown that this minimizes the shadow grid cast on CCD images. No grid artifacts are seen in the TRACE EUV images. The transmission of the filters was measured on orbit by taking rapid triplets of images using first both filters, then each one separately. Assuming the solar image does not change, the transmission of each filter can be estimated. The result is that both filters are the same and transmit 48%, 46%, and 42% at 171, 195, and 284 Å respectively, in reasonable agreement with figure 5.

The UV filters serve a different purpose. The UV channel is sensitive to solar emission over 1200–8000 Å. Four filters in the filter wheels (table III) are used in various combinations to image a variety of specific wavelengths. The 1216, 1550, and 1600 Å filters are used alone to image the H I Ly α line, the C IV resonance line doublet, and the UV continuum respectively. To further isolate

Table III. Focal plane filter wheels.

Filter Wheel 1 (Fwd):	
Pos. 1	Open
Pos. 2	1600 Å
Pos. 3	Al
Pos. 4	1550 Å
Filter Wheel 2 (Aft):	
Pos. 1	Open
Pos. 2	1216 Å
Pos. 3	Al
Pos. 4	Fused Silica

the C IV lines a third image (referred to as a 1700 Å image) is made by using the 1600 Å and fused silica filters in tandem (see figure 9). An image of the C IV emission is then generated by a linear combination of the 1550, 1600, and 1700 Å images (Handy et al., 1998). The fused silica filter is used for "white light" (WL) images.

2.2. CCD CAMERA

The focused image is recorded with a CCD detector. The CCD was manufactured by Lockheed Martin Fairchild Systems and is a front-illuminated 1024×1024 array of 21 μm pixels. It is an MDI flight spare device, sensitive to wavelengths $\gtrsim$ 4000 Å. To sensitize the CCD to UV and EUV wavelengths, the front surface of the CCD was coated with 1500 Å of lumogen, a coating that fluoresces at visible wavelengths when hit by UV and EUV photons (Deeg and Ninkov, 1995; Kristianpoller and Dutton, 1964). The quantum efficiency of the lumogen coating was measured on witness samples and CCDs coated together with the flight units (table V) (Catura et al., 1998). The quantum efficiency is shown in figure 10.

A series of tests were run at the Stanford Synchrotron Radiation Laboratory (SSRL) to determine the effects of high levels of UV and EUV radiation on the response of the lumogen (Catura et al., 1998). The tested CCDs were subjected to an incident beam at 171 Å, the highest energy emission TRACE observes. The results

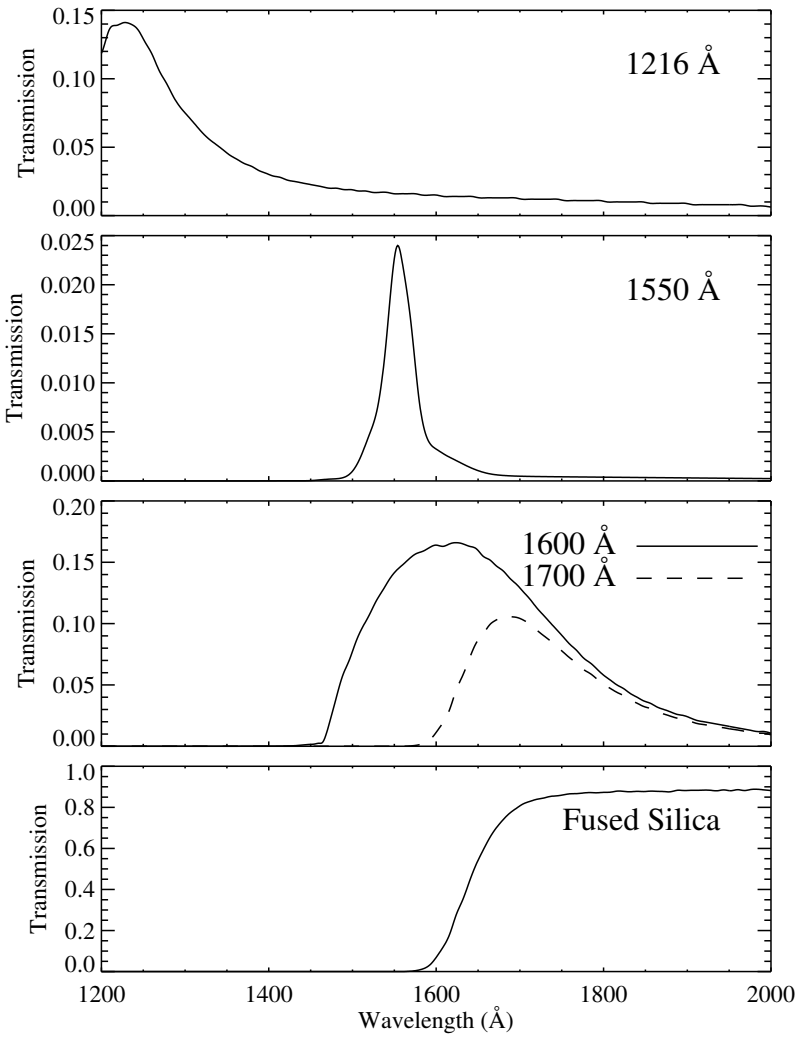

Figure 9. The UV filters used in TRACE. The 1700 Å filter is a combination of the 1600 Å filter and the fused silica filter. White light (WL) exposures are made through the fused silica filter. The transmission of the fused silica is ≈ 90% out through 7000 Å.

of the test indicated that the lumogen would suffer a measurable drop in sensitivity within the first year of observation, with an e-folding dose of approximately 10^{10} photons/pixel. In practice, however, the decrease in sensitivity on orbit has been substantially less than predicted, at the level of a 5–10% in the center of the EUV channel fields of view (see section 2.4.1).

Table IV. CCD camera parameters

Full Well	450,000 electrons
Dark current	1.2 electrons sec^{-1} @ −57 C
Linearity	± 1%
Readout rate	500k pixels/sec
Power	6.7 Watts
Amplifier gain	12 e/DN, amplifier A (default)
	42 e/DN, amplifier B
Read noise	20 electrons
Resolution	12 bits
ADC Offset:	86 DN (1 × 1 binning)

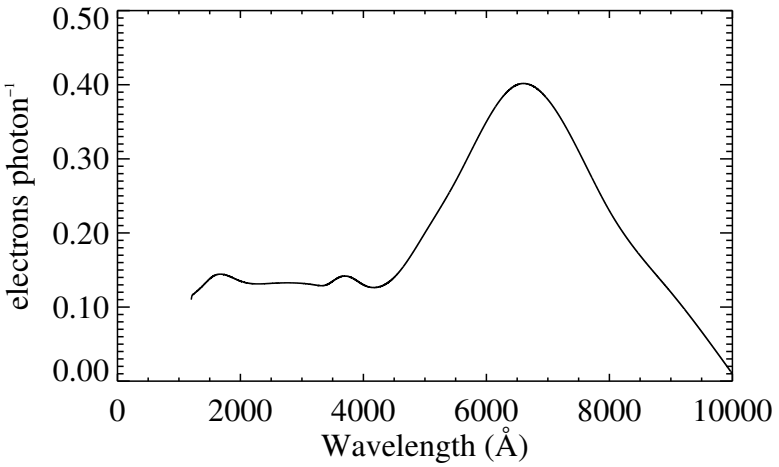

Figure 10. The response of the TRACE CCD in the UV and visible spectrum. The sharp rise in quantum efficiency centered near ∼ 6500 Å is the intrinsic response of the CCD to visible light. CCD sensitivity at wavelengths shortwards of 4000 Å is due to the lumogen coating.

2.3. Instrument response

TRACE images plasmas at a range of temperatures from 6×10^3–1×10^7 MK, spanning a range of the solar atmosphere from the photosphere through the chromosphere and transition region into the corona (table I). The combined throughput of the optics, mirror

Table V. TRACE CCD response at selected wavelengths. The measurements were made at the Lockheed Martin ATC facility on CCDs coated along with the flight units.

Wavelength (Å)	Quantum Efficiency (electrons photon^{-1})
171	0.09
284	0.08
304	0.08
1215	0.09
1605	0.15

reflectivities and CCD are shown in figures 11 and 13. In figure 12 the temperature response of the three EUV channels is modeled with the CHIANTI code (Dere et al., 1997). This model assumes coronal abundances as described by Feldman (1992) and ionization equilibrium as described by Arnaud and Raymond (1992).

A few comments on these curves are in order. The 171 channel is centered slightly above 173 Å, but is usually called 171 to be consistent with the terminology of EIT on SOHO. The 284 Å channel has some residual transmission at 304 Å He I, but the exact amount was not measured accurately in the pre-flight calibration due to spectral contamination at that wavelength by a second-order line. TRACE 284 Å images in quiet sun show some structures in common with EIT 304 Å images, confirming some leakage. The 1216 Å Ly α channel has a large contribution from UV continuum at wavelengths beyond 1500 Å. On the solar disk, more than 50% of the light in a TRACE 1216 Å image is really continuum, except perhaps in flares. Prominences above the limb are nearly pure Ly α, however; this has been shown by comparing test images taken with both the 1216 and 1600 Å filters in series with simultaneous normal 1216 and 1600 Å images.

TRACE 1550 and 1600 images contain significant contributions both from the C IV lines at 1548 and 1550 Å and from neighboring continuum and lines. Neither is a "C IV" image or a "UV continuum" image. At a glance, both resemble an image taken in the center of the Ca II K line with a bandpass of a few Angstroms (Lites et al., 1999). A TRACE 1700 Å image contains no C IV due to the absorption of the fused silica, so it is dominated by UV

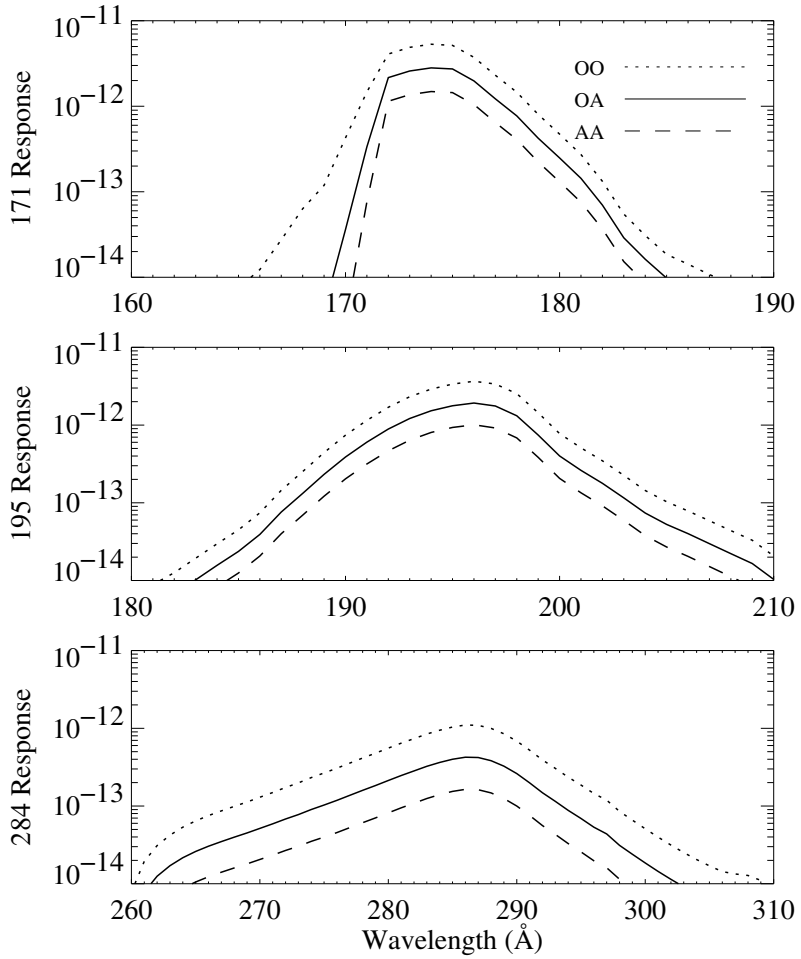

Figure 11. Spectral response of the EUV quadrants, in units of electrons sr cm^2 photon^{-1} pixel^{-1}. (Convolving a solar spectrum with the response function will yield the expected TRACE count rates). The nominal filter combinations are shown: "O–O" ("open-open"), with no Al focal plane filters in the light path, "O–A" ("open-Al"), with one focal plane filter is in the light path, and finally "A-A" ("Al-Al"), with both focal plane filters in the light path.

continuum, with some weak emission and absorption lines contributing. It resembles a visible image of the temperature minimum taken in the CN bandhead or the wings of the K line. Handy et al. (1998) describe how to estimate the actual C IV intensity from a set of 1550/1600/1700 images; less accurate estimates can be made from any pair of these. The WL response of TRACE has

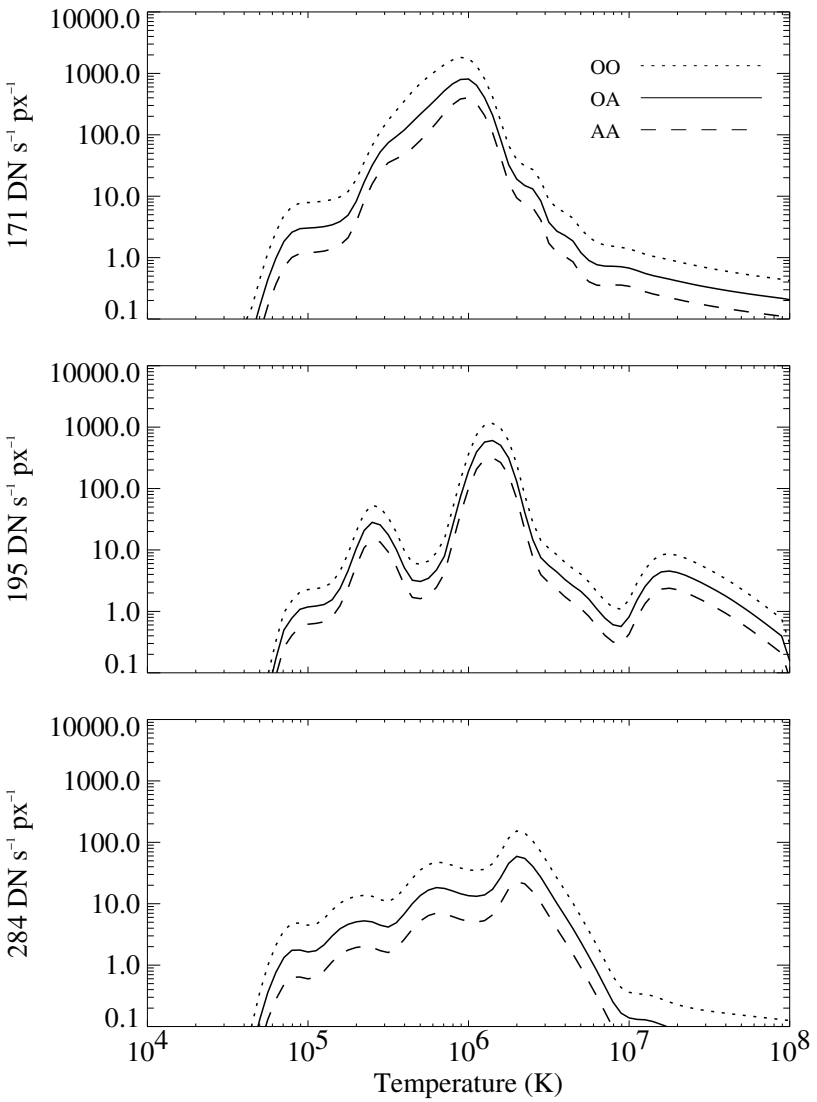

Figure 12. Signal at the CCD from each of the TRACE EUV quadrants as a function of source temperature for a solar emission measure of 10^{44} cm^{-3}.

significant contributions from 1700 Å to 1 μm. The transmission of the UV entrance filter decreases from 1700 to 5000 Å at a rate similar to the increase in the solar spectrum. Hence, TRACE WL images show solar granulation, sunspots and faculae similar to visible images in the blue. Their UV component is not negligible,

however; emission features are seen in modest flares on the disk and occasionally even above the limb.

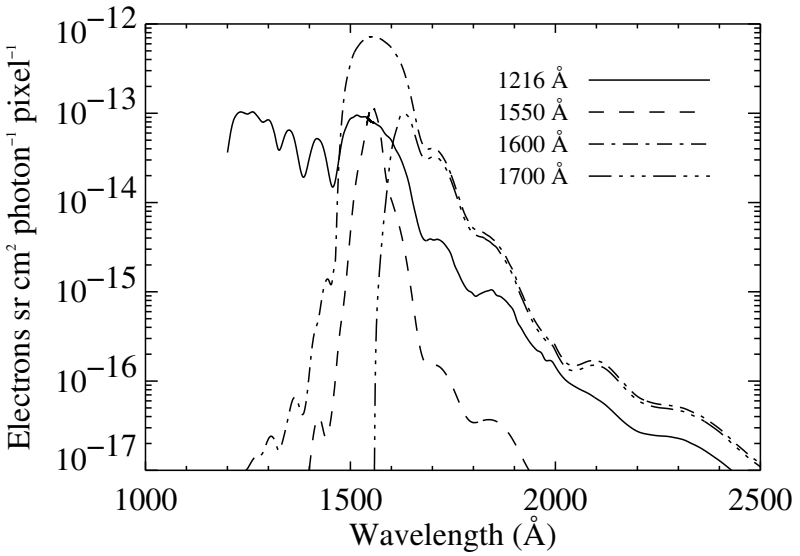

Figure 13. The combined response of the UV optics and CCD quantum efficiency in the TRACE instrument.

2.4. On-orbit characterization

Efforts to characterize the on-orbit instrument performance have been ongoing since the initial commissioning phase. Some specifics of that work-in-progress follow.

2.4.1. *CCD flat field and lumogen performance*

On-orbit flat fields of the TRACE CCD and optics in WL and 1700 Å wavelengths, using the the Kuhn-Lin flat-field algorithm (Kuhn et al., 1991) have been generated. The Kuhn-Lin algorithm requires taking a number of images at slightly shifted locations on the CCD with the image out of focus to reduce contrast. This shifting is done with the secondary mirror PZTs, which shift the images up to $\pm$ 15 arc seconds. This method works well for the WL channel, which is of relatively low contrast (figure 14). For the 1700 Å flat fields, offset pointing by the spacecraft is used to increase the shifts to $\sim$ 80 arc seconds.

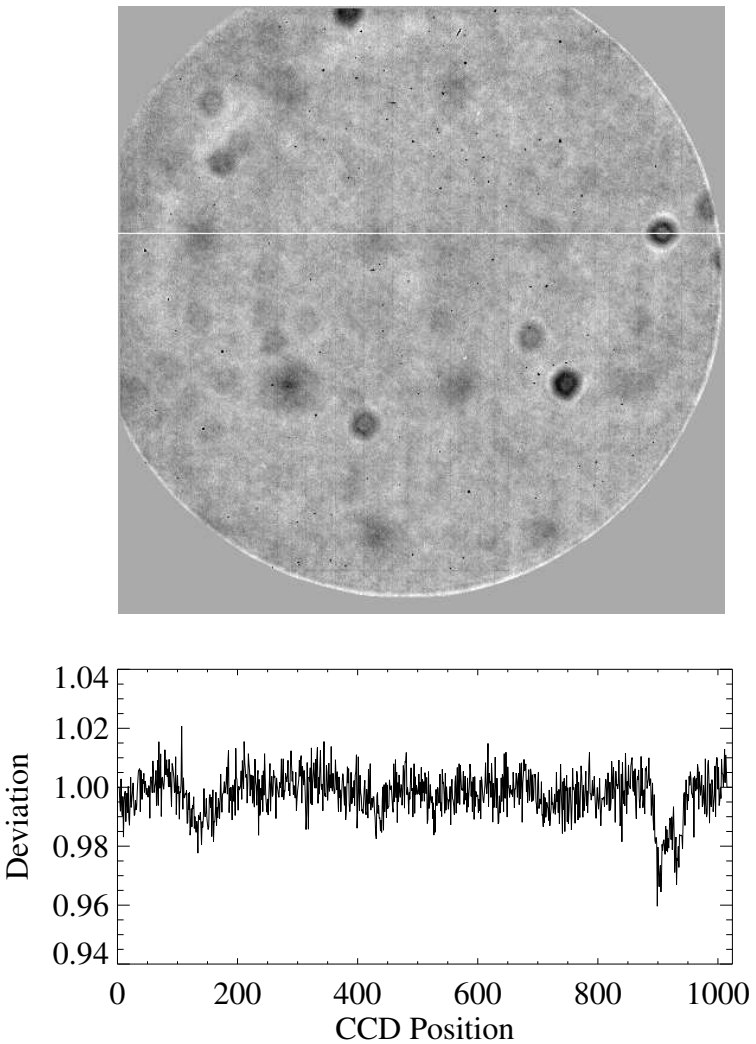

Figure 14. The TRACE flat field in the WL channel for 13 January 1999. Typical excursions across the field show variations of $\sim \pm$ 1% peak-to-peak. The vignetting around the edges is due to the masking of the CCD by the filter wheels. Some of the large blobs are dust particles on the fused silica filter; others are intrinsic to the CCD. The horizontal white line in the image indicates where the plot is taken.

The WL flat field, which has been normalized to a value of 1.0, is quite flat and of good quality, in the sense that it corrects WL images to high accuracy. A typical line through the flat field (c.f., figure 14) shows variations at the $\pm$1.0% peak-to-peak level. The

flatness and quality has changed very little since launch, with a difference image of two flat fields taken 7 months apart showing $\pm 1.0\%$ peak-to-peak variations, the same range as the flat fields themselves.

Several features are evident in the WL flat field of figure 12. There are many small dark spots of $\sim$ 1–3 pixels across with intensities of 20–80% of the normalized field. These dark spots were present on the CCD prior to launch and correct well in the WL images. In the near future most of these will be treated on board as bad pixels, to be replaced by a good nearest neighbor, because they interact poorly with the on board data compression algorithm.

Larger spots ($\sim$ 50–60 pixel diameter with an intensity of $\sim$ 96–98%) are evident on the WL flat field. These are most likely shadows of dust particles on the fused silica filter in the aft filter wheel. They disappeared when a WL flat field was generated from images for which no fused silica filter was used. However, another set of less well focused, larger ($\sim$ 80 pixels), and lower contrast ($\sim$ 97–99% intensity) spots then became apparent as a uniform array on the CCD. This regular array of spots was visible prior to launch at several wavelengths during CCD testing and is believed to be a CCD fabrication artifact. All of these features correct well in the WL images.

A pair of bad partial rows (CCD columns actually) are present in the WL flat field. In addition, vertical and horizontal dark lines are seen every 24 pixels at very low contrast. These are a CCD fabrication artifact.

The 1700 Å flat field (figure 15) shows some degradation in the relative response across the field of the CCD in the center. Although 30 images were utilized in the analysis of the flat field, most of the CCD structure is not resolved at this wavelength due to higher contrast, lower count rates, and changing structure in the original images when compared to those in WL. Despite defocusing, the 1700 Å images in quiet sun have network features three times brighter than average intensity. However, the pair of bad partial pixel rows observed in the WL flat field is also present in the 1700 Å flat field. The 1700 Å flat field for 7 January 1999 demonstrates a degradation of about 5–8% in the center region of the CCD with a small portion degrading up to $\sim$ 10%. A 1700 Å

flat field from 9 October 1998 displayed about a 2–5% relative degradation in the same region.

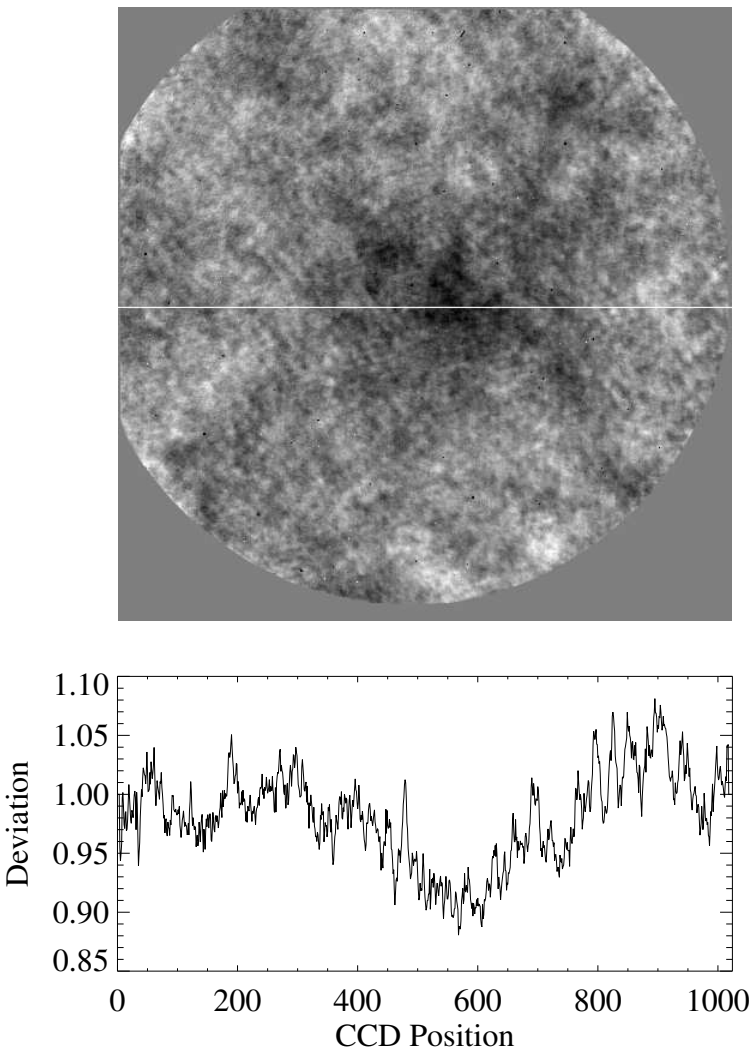

Figure 15. The TRACE flat field in the 1700 Å channel. The flat field is somewhat mottled in appearance compared to the WL.

This relative degradation in response across the field is probably occurring in the lumogen coating on the front of the CCD. A similar loss has been noted near the CCD center in EUV images of loops on the limb when compared to images with the limb moved to regions near the outer, non-degraded portions of the CCD area. The decrease in lumogen sensitivity near the center of the CCD

is probably a result of damage by the accumulated EUV dosage. A much higher level of lumogen degradation was anticipated from an experiment run at the SSRL (Catura et al., 1998).

Efforts are ongoing to generate satisfactory flat-field images for the other lines. The EUV wavelengths are particularly resistant to this method, as they are of extremely high contrast with much of the image at a very low count rate.

2.4.2. *Image coalignment*

The telescope was designed to provide consistent coalignment between all channels of the instrument. Slight offsets are caused by changes in best focus position of the secondary mirror and by wedge and tilt in the UV filters. Typical offsets are shown in table VI. These offsets are derived from limb observations and flare observations visible in the WL channel. The analysis software used to prepare the data (e.g., *SolarSoft,* Freeland and Handy (1998)) contain a set of offsets as a function of mission day.

Table VI. Typical image pixel offsets of the different wavelength channels relative to the WL channel. The offsets for the three EUV channels (171, 195, and 284 Å) are the same and are only listed once. To align an EUV image to a WL image, shift the image right 4.3 pixels and down 7.2 pixels.

Wavelength Channel	Image offset (pixels)
EUV	$(-4.3, 7.2)$
1600 Å	$(1.2, -1.2)$
1700 Å	$(1.2, -1.8)$
1550 Å	$(0.5, -1.3)$
1216 Å	$(6.2, -2.5)$

2.4.3. *Focus and Image Quality*

The TRACE telescope focus is adjustable over a wide range by a mechanism which moves the secondary mirror along the optical axis. The depth of focus may be defined as the focal shift for which the geometric blur diameter equals one pixel on the CCD. For the UV aperture, this corresponds to 5 steps of the focus mechanism,

while for the slightly larger EUV quadrants, it is about 3.5 steps; the total range is ±90 steps. Every month a set of images at different focus positions is taken in each wavelength, and the position of best focus is estimated from the image sharpness. Visual and numerical estimates (based on RMS values of $d\mathrm{I}/dx$ and $d\mathrm{I}/dy$) give consistent results. The EUV wavelengths all come to focus at the same position, within the uncertainty of the measurements, about ±2 steps. The WL, 1550, 1600, and 1700 Å images focus close together in a repeatable pattern, shifted about 8 steps from the EUV focus. 1216 Å focus is measured only from prominence images, because the longer wavelength leakage seen on the disk has a different focus. The Lyman alpha focus is 6–10 steps from that of the other UV wavelengths; presumably this is due to temperature gradients in the front window and the strong temperature dependence of the index of refraction of MgF_2 at 1216 Å.

During normal observing, the focus mechanism moves to the appropriate UV or EUV focus automatically for each frame. No position is more than 12 steps from the nominal center of the range which was set during ground testing of the telescope. In the first year of full-sun observing, none of the best focus positions changed significantly, except possibly 1216 Å, which may have a seasonal variation with the temperature gradient of the front window. The thermal effects on 1216 Å were much more significant during eclipse season. Just after an orbital sunrise, the focus was off by more than 20 steps from normal; more than 30 minutes was required for the focus to return to normal as the thermal transient died out. The other UV wavelengths only shifted a few steps at sunrise and returned to normal in less than 15 minutes.

TRACE images in 1550, 1600, and 1700 Å are limited in image quality by the pixel size over the entire field of view; this is evident from the appearance of small bright points in both quiet and active sun. Diffraction-limited sampling would require pixels smaller than 0.30 arc seconds. In the EUV, the finest loops and smallest flare kernels also suggest pixel-limited image quality. Some image sets have been taken with half-pixel shifts introduced by tilting the secondary mirror (see section 2.5). These may be analyzed to produce an estimate of the point spread function and/or images with enhanced resolution, but results to date are inconclusive.

2.5. Pointing and image stabilization

The Guide Telescope (GT) and Image Stabilization System (ISS) perform two primary functions. In a cooperative mode with the spacecraft attitude control system (ACS), the GT directs pointing maneuvers to desired solar targets. The ISS provides jitter removal to $\lesssim$ 0.1 arc second RMS based on error signals from the GT.

The GT has a 2.5 cm aperture and an effective focal length of 187 cm. It forms a filtered (5600 Å with a FWHM of 500 Å) image of the Sun which falls onto a limb sensor unit that consists of four pairs of photo diodes mounted at 90 degree intervals (Zimbelman et al., 1995). The intensity difference between opposite diodes is a linear displacement error signal with a range of $\pm$120 arc seconds. Signals are sent from the instrument to the spacecraft ACS which adjusts the pointing to keep the limb sensor centered. A pair of independently rotatable wedge prisms are mounted between the entrance filter and the objective lens to enable the optic axis of the telescope to be deflected in any direction within a cone of 1 degree half-angle centered about the optic axis of the main telescope. The ACS is continually adjusting the pointing of the spacecraft to keep the limb sensor centered, which results in the main telescope field of view moving to the desired offset location. The wedges are rotated in discrete steps, which means that the possible pointing locations are a lattice with maximum spacing of about 60 arc seconds. Moving from one position on the disk to another typically takes about 30 seconds and is less than 2 minutes in the most extreme case.

The secondary mirror of the main telescope is mounted on a steering mechanism that uses 3 piezoelectric transducers (PZTs) to tilt the mirror over a range of about $\pm$130 arc seconds in each axis, corresponding to $\pm$42 arc seconds in the solar image at the CCD. Difference signals between opposite diodes in the GT sense image movements of less than 0.05 arc seconds and send the resultant error signal to the PZTs to stabilize (by recentering at a high frequency) the image. The 3 dB bandwidth of the servo is about 15 Hz. Motions of the three PZTs are constrained so that the mirror only tilts and telescope focus is maintained. A schematic of the pointing and image stabilization systems is given in figure 16.

The ISS is an open-loop control system in the sense that the error signal is derived from the GT rather than from motions of the

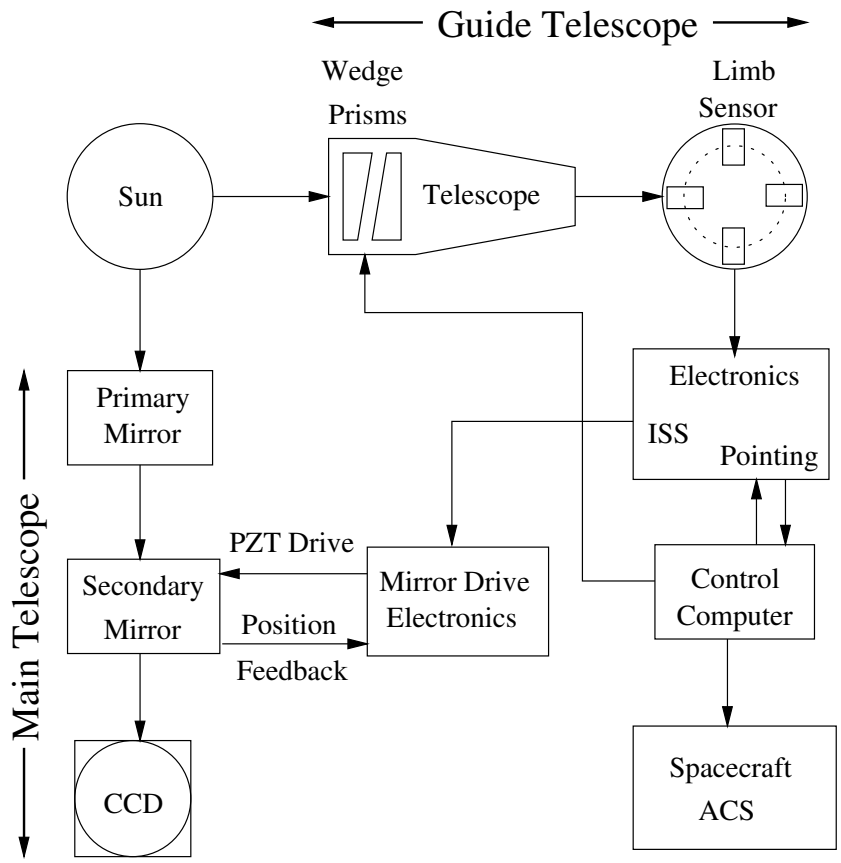

Figure 16. The TRACE pointing system.

image in the main telescope. On-orbit calibration of the applicable transfer functions enables this approach to work very well. In addition, the PZT actuators are part of a closed-loop servo in which the feedback signals are derived from strain gauges incorporated into the actuators. Using the strain gauges, accurate and repeatable image offsets from the home position can be commanded while jitter compensation continues; these are used for flat fields and sub-pixel imaging tests as described above.

The performance of the ACS and ISS have been measured on-orbit by digitizing and storing the GT error signals and PZT drive signals at a rate of 100 Hz. These show that the short term pointing stability is usually better than 0.25 arc seconds RMS before correction by the ISS, and better than 0.1 arc seconds after

correction. The worst transient is caused by the quadrant sector shutter, which causes pitch and yaw errors of about 4 arc seconds lasting a few seconds; these are corrected by the ISS to about 0.2 arc seconds. The filterwheels and shutter cause transients less than 0.1 arc second. Unlike SOHO, the TRACE reaction wheels are not causing measurable jitter; the only spacecraft jitter source detected is the solar panel first mode at 4 Hz, which is excited at a very low level by the quadrant shutter.

The GT cannot detect rotation of the solar image on the limb sensor. If the spacecraft rolls about the line of sight, then the image rotates on the CCD camera. In addition, if the pointing is offset from disk center, the GT/ISS/ACS system converts roll into a translation of the image parallel to the solar limb. The spacecraft senses roll from the Earth's magnetic field, and some slow drift in roll occurs during the orbit. Another source of pointing drift, thermal bending of the GT mounting, has also been found; this is typically a few arc seconds peak to peak and is periodic with the orbit. It has proven difficult so far to separate these effects and to calibrate the roll sensors accurately. As a result, TRACE absolute pointing coordinates are uncertain by a few arc seconds.

2.6. On-board control and data processing

The instrument computer system consists of 2 processors: the control computer (CC) and the Data Handling Computer (DHC). The CC is an i86 architecture machine with a radiation hardened 80C86 processor and additional electronics, some standard and some custom. The DHC is a custom image processor based on the AMD 2910 bit-slice architecture. The CC controls electromechanical components, manages the spacecraft command and housekeeping interfaces, and maintains the cadence of all operations including science observing sequences. The DHC receives raw data from the camera system, processes it, and outputs formatted data to the spacecraft's bulk memory via a high speed serial interface. Based on information supplied by the CC, the DHC performs various operations on the image data including flare detection, exposure evaluation, time averaging, spatial averaging, sub-field extraction, and JPEG compression.

2.6.1. *Science Sequencer*
The CC contains an operating system which maintains the general integrity of the instrumentation and an application which operates the instrumentation through a variety of programmable scenarios called observing sequences. The series of modules which realize an observing sequence is called the sequencer. The sequencer includes standard arithmetic capabilities, test and branching instructions, timing capabilities, and instrument specific instructions for manipulating the hardware and exchanging information with the DHC. There are two key instructions for observing control. These are the FRAME and STTG instructions. The FRAME instruction takes a picture using the parameters in a frame definition block (FDB). The STTG instruction causes the spacecraft to point to a position on the sun. In practice, a sequence is a list of general purpose instructions to control repetition and branching that bracket FRAME and STTG instructions to take desired images at particular solar coordinates.

The sequencer provides a number of parameters that indicate the current condition of the instrument. These can be used within the sequence to control branching or to invoke exit conditions. Some of the built-in parameters are listed in table VII.

2.6.2. *On-Board Processing*
During a camera readout cycle, data is dumped directly to a DHC memory page. When the readout is finished, the DHC hardware asserts a level that the DHC firmware can detect. The DHC polling loop sees this level and begins a program that processes the image data. Data processing occurs in two phases. Phase I examines the image data for any events that have been requested by the FDB. Event results are sent to the CC, which in turn commands the DHC to initiate phase II. Phase II performs the image processing indicated by the FDB and transfers the image data to the spacecraft. In the CC, the sequence resumes upon completion of phase I using the results as needed to control the logic flow.

2.6.3. *Sensor Safety*
The first phase I function is an overdosage safety check, which is automatically applied to all EUV images. The function bins the camera data to 128×128 and makes a histogram of the binned data. Using the histogram, it determines if there are ex-

Table VII. Built-in Sequencer Parameters

Parameter	Description
SAA, HLZ	The SAA and HLZ flags indicate if the spacecraft is in the South Atlantic Anomaly or High Latitude Zones in which there is increased particle radiation. Sequences often restrict the types of exposures taken in these areas.
CBS	The chronological buffer status flag indicates the amount of data currently in the spacecraft's bulk memory. Sequences can reduce their cadence, pause, or terminate if the buffer is nearly full.
FEF, SEF, TEF	These flags indicate if a flare, super flare, or transient event has been detected. The event detection mechanism is described in section 2.6.5.
MXC, MXR, MXV, MNC, MNR, MNV	These parameters give the coordinates of, and counts at, the most recently requested I_{max} and I_{min}.
PRI	The sequencer contains a 2 level priority scheme. High priority sequences can be interrupted only by high priority sequence starts.

cessive counts in the detector. The threshold that defines excess is adjustable. If a specified number of sequential images are taken which exceed this threshold, the CC terminates the sequence. The sequence can be resumed by ground or timeline command. This feature is designed to protect the CCD lumogen coating from excessive damage by intense solar events. The check can be disabled by ground command.

2.6.4. *Area Processing*
The FDB can specify different image processing for the full camera field of view and 2 sub-areas. The sub-areas can be centered at the I_{min} or I_{max} of an earlier image, the center of the CCD, or any arbitrary point within the image. Sub-areas must be rectangular with each dimension restricted to multiples of 64 pixels.

2.6.5. *Event Detection & Extrema*
Phase I performs event detection and extrema location based on requests in the FDB. Event detection includes flare, super flare, automatic exposure control (AEC), and transient detection. The first

three events use a method which makes a cumulative histogram of the image data and examines a particular bin in the histogram to determine if the event has occurred. For example, a flare occurs if a sufficient number of pixels exceed a certain level. AEC similarly uses the histogram to determine if the CC should adjust the next exposure duration up or down based on the population at the low and high ends of the histogram.

Transient detection looks for relative changes in the image. The FDB specifies a multiplier that is applied to an image. If the next image has a sufficient number of pixels that exceed the enhanced image, then a transient event has happened. Transient detection can also be applied to time averaged image sets. In addition there is a capability to respond to relative darkening.

2.6.6. *Binning, cropping and time averaging*
Each area can specify binning and cropping. Image data can be cropped to any rectangle whose sides are multiples of 64 pixels. Cropped or full image data can be binned at 2×2, 4×4, or 8×8. Binned data is averaged to retain a 12-bit data value. Any number of images from 2 to 16 can be time averaged.

2.6.7. *Compression*
Image data can be transferred directly to the spacecraft as 16-bit data words or compressed prior to transfer. Compression methods include packing to 12-bits, table lookup to 8-bit data, or 12 bit JPEG compression (Pennebaker and Mitchell, 1993). Different methods may be applied to each area. 15 different lookup tables are available. JPEG compression uses pre-loaded Huffman and quantization tables, i.e., the JPEG is not adaptive. Up to 4 Huffman tables and 64 quantization tables exist and different tables can be loaded to improve compression efficiency.

The pre-launch Huffman table, optimized for a mix of EUV and UV images, has worked satisfactory but tables optimized for actual TRACE images may be loaded for the second year of operation. The quantization table is a symmetrized version of the standard JPEG table and is scaled in the same manner to generate a range of quantization tables (64 available) to provide a range of qualities. 12 bit JPEG compression of a 1024×1024 image requires 2.5 to 4.5 seconds and smaller images scale according to area. Since the compression time per pixel is less than the transfer time to

mass memory per pixel, compression generally improves cadence. EUV images are routinely compressed to about 0.5 bits/pixel for active region movies while UV images, which generally have higher counts and entropy, are routinely compressed to about 2 bits/pixel. When highest quality is needed (i.e., for small scale faint features), a nearly lossless mode can be used which utilizes the JPEG code without a quantization table. This typically requires 3 to 5 bits/pixel in the EUV. Intermediate and lower quality images are also possible. A detailed report on the compression technique and performance is in progress (Shine, 1999).

3. Operations

3.1. Observing programs

The instrument field of view observes about 1/10th of the solar disk at a time. TRACE is best suited for continually monitoring within this field of view at a high temporal cadence. Higher time cadence is obtained by only taking a subset of the available wavelengths; often one of the EUV wavelengths, one UV wavelength and the WL channel for alignment with other data (see table VIII for typical exposure times in each channel). A sequence of this sort can achieve a temporal cadence of about 20–30 seconds. Such observations are then constrained by the available mass memory and telemetry. Spacecraft memory use is optimized by on-board 12-bit JPEG compression of data, with the level of compression being dependent upon wavelength and required image quality.

The high resolution of the instrument suggests that interesting work can also be done with larger fields of view: full disk mosaics, 1×5 mosaics of the central meridian and of the active region belts, and various combinations of fields of view to encompass the solar poles or east and west limbs. The baseline synoptic plan is to collect a set of full-disk mosaics in selected wavelengths at the discretion of the daily planner roughly once a week (more often when the SOHO/EIT instrument is not operating) and a central meridian scan in all wavelengths on most days. The latter is taken at the time of the SOHO/CDS synoptic program (Harrison et al., 1995) in the same area.

Table VIII. Typical exposure times for an active region. When binning is used (e.g. 2×2 binning in the 284 Å channel) exposure times are reduced by a factor of 4.

Wavelength Channel	Typical exposure time (sec)
173 Å	15
195 Å	15
284 Å	80 (20 in 2×2 summing)
1216 Å	1
1550 Å	14
1600 Å	0.5
1700 Å	5
WL	0.006

3.2. Mission operations

Observations are controlled by a *timeline* that is uploaded to the observatory, 5 days a week during regular observing and 3 times a week during eclipse season. TRACE is operated from the Experiment Operations Facility (EOF) at the NASA Goddard Space Flight Center (GSFC). The TRACE EOF is in the same building as the SOHO EOF and TRACE is treated as an additional SOHO instrument for operations planning. A team of scientists familiar with the TRACE observatory work on a rotating schedule as TRACE planners. They take part in the SOHO planning meetings and contribute to the SOHO calendar, Instrument Activity Plan, and synoptic image databases. Web displays of timelines, instrument status, and sample images from recent observations are generated automatically in the EOF. These are used by the distributed TRACE team and collaborators on SOHO, SXT and at ground-based observatories.

For the first 7 months a staff of TRACE scientists was continuously located at the EOF. During the eclipse season TRACE ran much simpler timelines and planning took place at the scientists' home facilities. Extended mission operations following the first eclipse season will again be done from the EOF at GSFC.

The TRACE weekly planner (and other operations team members) can be reached via email[1]. All inquiries for coordinated observing should be sent to this address.

3.3. Ground based tools

3.3.1. *Sequence control language*

The science sequencer described in section 2.6.1 contains all the capabilities required to realize TRACE science observations; however, it is not a particularly friendly language. Observers are isolated from it by ground based tools including a compiler. The sequence compiler allows the user to write sequences in a language similar to C. The sequence control language contains `while`, `for`, and `if` constructs and allows calls to sequences by name.

3.3.2. *Frame definition tool*

Frame definition blocks (FDBs) contain the detailed configuration of and processing steps requirements on the images taken in a sequence. There exists an FDB creation tool, driven by a graphic user interface, with which an observer can create new frames without referencing the detailed coding of the FDB.

3.3.3. *Timelines*

The software support tools include a program for generating the daily timeline. During regular observing a new timeline is run every day, and a longer 3-day timeline runs on weekends. The timeline includes all commands the spacecraft requires as well as those for the instrument. The TIMELINE program is a graphic user interface program that the observer uses to construct the daily science plan. The program allows point and click access to all sequences that are on board and to all legal telecommands. The program verifies the input and runs a simulation of the proposed timeline that includes a time history of the estimated usage of spacecraft bulk memory.

3.4. Orbital considerations

The TRACE observatory is in a sun-synchronous polar orbit of 600×650 km at an inclination of 97.8 degrees, following the

[1] `trace_planner@diapason.lmsal.com`

solar terminator. This orbit allowed continuous uninterrupted solar observing for the first 7 months after the launch on April 2, 1998, followed by a 3-month eclipse season. The spacecraft will subsequently cycle through periods of uninterrupted observing and eclipse seasons of about 9 months and 3 months, respectively, and will eventually precess into a long eclipse mode. The baseline mission plan was that the instrument would be powered down during eclipse season due to thermal and power constraints, but post-launch evaluation indicated that TRACE has ample power to run during eclipse season. TRACE was therefore left powered up and performed simple observations (full-disk mosaics and long-duration active region studies) during the first eclipse season. TRACE downlinks occur typically six times per day over some combination of over Wallops Island, Virginia; Poker Flat, Alaska; and McMurdo Bay, Antarctica.

The TRACE orbit is such that the instrument routinely passes through the South Atlantic Anomaly (SAA, Sherrill (1991)) and the auroral radiation belts. The SAA passage was anticipated prior to launch and on-board software was developed so that observations could pause during the predicted times of the SAA.

The high radiation zones are problematic for several reasons. Images taken during periods of highest intensity are overwhelmed by charged particle hits and are not scientifically useful. Further, these artifacts are high contrast and of high spatial frequency and do not compress very effectively, thus using up significant mass memory. Lastly, a high frequency of charged particle hits in the images affects the Automatic Exposure Control (AEC), resulting in unrealistically short exposure times after emerging from these regions. These effects are most obvious in the high contrast EUV wavelengths. The UV and WL images are less affected by the radiation belts, primarily because the exposures are shorter and the light levels are much higher.

To accommodate the SAA and high latitude zones (HLZs) of heavy radiation, flags were built into the flight software to allow pausing of image acquisition during passage through these regions. These regions are predicted by geometrical considerations and merged into the timeline. The HLZs were also mapped by analyzing the number of radiation hits in images returned from TRACE over a three week period with the HLZ flags disabled. These zones map out an annulus around the north and south magnetic poles,

somewhat equatorward and outside the polar auroral regions. The HLZs were then redefined as a range of magnetic latitudes for planning purposes.

Partway through the first observing season efforts were spent on radiation detection onboard the instrument, rather than depending on the predicted time of entry into the SAA or HLZs. The observing sequences monitor the intensity in the vignetted corners of the CCD. When this total intensity exceeds a threshold value, the image is assumed to be contaminated by radiation hits on the detector and observing is suspended until the monitored level drops to a more reasonable value. This method enables TRACE to obtain cleaner image sets because the predicted entry and exit times were not very accurate and did not account for the dynamic nature of the radiation zones. In addition, it requires much less daily effort by operations personnel.

4. Data management

4.1. TRACE DATA CENTERS

Data from the TRACE mission is freely available to all interested parties as soon as the data reaches the Data Centers, typically within 2 days of an observation. Data may be requested through email or via the web; small datasets are provided over the Internet. For large datasets the requester will be contacted to determine the best way to implement the request. All users are requested to register with the data center for informational purposes.

The TRACE data is accessible through several data centers in the USA and Europe. The primary locations are at the Lockheed Martin Advance Technology Center in Palo Alto, California (USA) and the Solar Data Analysis Center at Greenbelt, Maryland (USA). (See appendix A for web addresses.)

4.2. DATA ANALYSIS & CALIBRATION SOFTWARE

TRACE data is maintained and reformatted with the *SolarSoft* (SSW) library and IDL. The SSW library contains a suite of tools for analyzing and comparing solar and astrophysical data from TRACE and other solar observatories (Freeland and Handy, 1998).

A second option for browsing the data and movie-making is the ANA software library. ANA is a public domain package originally developed during the Solar Maximum Mission by Richard Shine and collaborators. In the past ten years, the ANA browser has become a very powerful tool for manipulating image data, especially high resolution solar movies and images from several different instruments (Hurlburt et al., 1997). With the browser, a user can quickly inspect individual images in a TRACE hourly raw data file. Interactive frame selection and movie-making tools can extract a customized movie datacube, which can be viewed on a workstation within minutes of receipt of the raw data.

A preliminary TRACE Analysis Guide (TAG) is being prepared to aid in data analysis. URLs for these analysis suites are listed in appendix A.

5. Conclusions

The TRACE observatory has, in the first season of observing, provided a look at the solar atmosphere at unprecedented spatial and temporal resolution. Images and movies from TRACE show a previously unimagineable level of structure and variability in the solar atmosphere from the temperature minimum to the high-temperature corona. Initial results are discussed by Golub et al. (1999) and the companion paper by Schrijver et al., this volume.

TRACE images solar plasmas in the EUV, UV and visible spectrum over an 8.5×8.5 arcminute field of view with a temporal cadence of $\gtrsim 3$ seconds. The TRACE observatory is capable of nearly continuous coverage due to the large on-board memory and numerous daily downlink passes. The amount of power available has permitted continuous observation through the eclipse season, providing unanticipated additional observing time. Flexible observing programs make it possible to collaborate with numerous other observatories including SoHO, *Yohkoh* and many ground-based observatories.

After nearly a year in orbit, both the spacecraft and the instrument are in excellent condition and the orbit is such that solar observing is possible for several years to come. The data collected are available without restriction.

6. Acknowledgments

This work was supported by contract NAS5-38099 with NASA Goddard Space Flight Center. We would like to acknowledge the very close working relationship established early on with the SMEX project at Goddard Space Flight Center. The ANA browser has been developed with support from NASA's Applied Information Services Research Program (Contract NAS8-39746) and Lockheed Martin Independent Research Funds.

We particularly acknowledge the teamwork and high level of technical expertise of several of our industrial subcontractors, including Luxel Corporation (Forbes Powell) for their thin-film EUV filters; Lawrence Livermore National Laboratories (Troy Barbee) for the EUV mirror multilayer coatings; Acton Research Corp. (Michael Laforge, Joe Oliver and Bruce Flint) for the UV Multilayer optics; H. Magnetics (Ralph Horber) for the mechanisms; Lockheed Martin Fairchild (Dick Bredthauer) for the CCDs and lumogen coatings; Wilc Instruments (Januz Wilczynski) for the figured primary and secondary mirrors; Raytheon Optical Systems (Paul Reid) for superpolishing the mirror surfaces; and NIST (Charles Tarrio) and Lucent Technologies (David Windt) for measuring the reflectivity of the EUV mirror coatings.

Appendix

A. TRACE information on the WWW

- The main TRACE web site:
  `http://vestige.lmsal.com/TRACE/`

- TRACE Data Analysis centers:
  `http://vestige.lmsal.com/TRACE/DataCenter/`
  `http://umbra.nascom.nasa.gov/TRACE/Data/trace_cat.html`

- The ANA data browser:
  `http://ana.lmsal.com/`

- IDL (Research Systems, Inc.)
  `http://www.rsinc.com/`

- The SolarSoft data analysis system
  `http://www.lmsal.com/solarsoft/`

- The TRACE Analysis Guide (TAG)
  `http://vestige.lmsal.com/TRACE/Public/siteinfo.htm`

- IMD—Multilayer optical properties: modeling and curve-fitting
  `http://www.bell-labs.com/user/windt/idl/`

- Atomic scattering factors used in modeling the thin-film EUV filters
  `http://www-cxro.lbl.gov/`
  `http://www-phys.llnl.gov/V_Div/scattering/asf.html`

References

Arnaud, M. and J. Raymond: 1992 *Ap. J.* **398**, 394.

Barbee, T. W., J., J. W. Weed, R. B. Hoover, M. J. Allen, J. F. Lindblom, R. H. O'Neal, C. C. Kankelborg, C. E. Deforest, E. S. Paris, and J. Walker, A. B. C.: 1991, *Opt. Eng.* **30**, 1067.

Catura, R. C., D. W. Duncan, L. Shing, T. D. Tarbell, and C. J. Wolfson: 1998, *Proc. SPIE*, 291.

Cheimets, P., J. Bookbinder, W. Davis, and L. Golub: 1998a, *Proc. SPIE*, 28.

Cheimets, P., J. Bookbinder, E. Deluca, D. Caldwell, W. Davis, and L. Golub: 1998b, *Proc. SPIE*, 96.

Damè, L., M. Martic, W. A. Brown, M. E. Bruner, K. Strong, Y. Suematsu, S. Tsuneta, and B. Schmieder: 1996, *Advances in Space Research* **17**, 189.

Deeg, H.-J. and Z. Ninkov: 1995, *Op. Eng.* **34**, 43.

Delaboudinière, J. P., G. E. Artzner, J. Brunaud, A. H. Gabriel, J. F. Hochedez, F. Millier, X. Y. Song, B. Au, K. P. Dere, R. A. Howard, R. Kreplin, D. J. Michels, J. D. Moses, J. M. Defise, C. Jamar, P. Rochus, J. P. Chauvineau, J. P. Marioge, R. C. Catura, J. R. Lemen, L. Shing, R. A. Stern, J. B. Gurman, W. M. Neupert, A. Maucherat, F. Clette, P. Cugnon, and E. L. Van Dessel: 1995, *Solar Phys.* **162**, 291.

Dere, K. P., E. Landi, H. E. Mason, B. C. Monsignori Fossi, and P. R. Young: 1997, *Astron. Astrophys. Suppl.* **125**, 149.

Domingo, V., B. Fleck, and A. I. Poland: 1995, *Solar Phys.* **162**, 1.

Feldman, U.: 1992, *Physica Scripta* **46**, 202.

Freeland, S. L. and B. N. Handy: 1998, *Solar Phys.* **182**, 497.

Golub, L., J. Bookbinder, E. DeLuca, M. Karovska, H. Warren, C. J. Schrijver, R. Shine, T. Tarbell, A. Title, J. Wolfson, B. Handy, and C. Kankelborg: 1999, *Rev. of Plasma Phys.*, in press.

Golub, L., M. Herant, K. Kalata, I. Lovas, G. Nystrom, E. Spiller, and J. Wilcyznski: 1990, *Nature* **344**, 842.

Handy, B. N., M. E. Bruner, T. D. Tarbell, A. M. Title, C. J. Wolfson, M. J. Laforge, and J. J. Oliver: 1998, *Solar Phys.* **183**, 29.

Harrison, R. A., E. C. Sawyer, M. K. Carter, A. M. Cruise, R. M. Cutler, A. Fludra, R. W. Hayes, B. J. Kent, J. Lang, D. J. Parker, J. Payne, C. D. Pike, S. C. Peskett, A. G. Richards, J. L. Culhane, K. Norman, A. A. Breeveld, E. R. Breeveld, K. F. A. Janabi, A. J. McCalden, J. H. Parkinson, D. G. Self, P. D. Thomas, A. I. Poland, R. J. Thomas, W. T. Thompson, O. Kjeldseth-Moe, P. Brekke, J. Karud, P. Maltby, B. Aschenbach, H. Brauninger, M. Kuhne, J. Hollandt, O. H. W. Siegmund, M. C. E. Huber, A. H. Gabriel, H. E. Mason, and B. J. I. Bromage: 1995, *Solar Phys.* **162**, 233.

Hurlburt, N. E., R. A. Shine, and T. D. Tarbell: 1997, *Proc. SPIE* **3017**, 165.

Kristianpoller, N. and D. Dutton: 1964, *Appl. Op.* **3**, 287.

Kuhn, J. R., H. Lin, and D. Loranz: 1991, *PASP* **103**, 1097.

Lites, B. W., R. J. Rutten, and T. E. Berger: 1999, *Ap. J.*, in press.

Pennebaker, W. B. and J. L. Mitchell: 1993, *JPEG Still Image Data Compression Standard*, Van Nostrand Reinhold.

Scherrer, P. H., R. S. Bogart, R. I. Bush, J. T. Hoeksema, A. G. Kosovichev, J. Schou, W. Rosenberg, L. Springer, T. D. Tarbell, A. Title, C. J. Wolfson, I. Zayer, and The MDI Engineering Team: 1995, *Solar Phys.* **162**, 129.

Sherrill, T. J.: 1991, *S&T* **81**, 134.

Shine, R. A.: 1999, *Solar Phys.*, in prep.

Strong, K., M. Bruner, T. Tarbell, A. Title, and C. J. Wolfson: 1994, *Space Science Reviews* **70**, 119.

Tarbell, T. D., M. Bruner, B. Jurcevich, J. Lemen, K. Strong, A. Title, J. Wolfson, L. Golub, and R. Fisher: 1994, in *Proc. of the Third SoHO Workshop — Solar Dynamic Phenomena and Solar Wind Consequences 26–29 September 1994*, 375.

Walker, A. B. C., J. F. Lindblom, R. H. O'Neal, M. J. Allen, J. Barbee, T. W., and R. B. Hoover: 1990, *Opt. Eng.* **29**, 581.

Windt, D. L.: 1998, *Comp. in Phys.* **12**, 360.

Zimbelman, D., J. Wilmot, and S. Evangelista: 1995, in *Proc. of the Ninth Annual AIAA/USU Conference on Small Satellites, September 18–21, 1995.*